A Lattice-Boltzmann model for simulating bedform-induced hyporheic exchange

Davide Dapelo[1], Stefan Krause[2,3,4], Jesus D. Gomez-Velez[5], John Bridgeman[1]

[1]Department of Civil Engineering and Industrial Design, School of Engineering University of Liverpool, Liverpool, United Kingdom.

[2]School of Geography, Earth and Environmental Sciences, University of Birmingham, Birmingham, United Kingdom.

[3]11. Ecologie des Hydrosystèmes Naturels et Anthropisés (LEHNA), Université Claude Bernard Lyon 1, Lyon, CNRS, ENTPE, UMR5023, 69622, Villeurbanne, France.

[4]Institute of Global Innovation, University of Birmingham, Birmingham, United Kingdom.

[5]Climate Change Science Institute & Environmental Sciences Division, Oak Ridge National Laboratory, Oak Ridge, TN, USA.

Key Points:

- Lattice-Boltzmann model successfully represents bedform-induced hyporheic exchange flow
- A fully-coupled surface-subsurface model for HE is proposed
- temporal variability in hyporheic flow patterns is observed

Corresponding author: D. Dapelo, `d.dapelo@liverpool.ac.uk`

Abstract

The Lattice-Boltzmann (LB) method is applied here for the first time to simulate bedform-induced hyporheic exchange flow in a reduced complexity model. The flexibility of the LB allows surface and hyporheic flows to be resolved together, in contrast to other approaches for similar model domains, in which surface flow is usually solved independently, and then the solution of the surface flow provides the boundary conditions to model the hyporheic exchange flow. At the same time, the superior computational efficiency of LB allows the use of Large Eddy Simulations within transient simulations. Numerical results show a faithful reproduction of pressure along the bedform surface—especially, the pressure drop leeward to the dune. Results also show short-time-dependent phenomena which were previously described only in the context of DNS studies over reduced-size computational domains. Short-time-dependent phenomena include pressure oscillations and time-dependence of hyporheic zone morphology, with the latter eventually extending beyond the limits of a single bedform element.

1 Introduction

Hyporheic exchange fluxes (HEF) play an important role in riverine environments as they affect streambed and river temperature dynamics (Wu et al., 2020), stream metabolism and biogeochemical cycling, with deep implications in ecosystem resilience (S. Krause et al., 2013). The spatial patterns and temporal dynamics of HEF are controlled by streambed topography and sediment properties (e.g., hydraulic conductivity patterns) and hydrodynamics and hydrostatic forcings from the surface flow. The morphology of stream bedforms and river corridor features such as meanders, ripples, dunes, gravel bars and pool-riffle structures create nested HEF patterns at the interface between surface and groundwater (S. Krause et al., 2022).

In addition to site-specific field studies (Marçais et al., 2018; Zarnetske et al., 2011; S. Krause et al., 2013; Angermann et al., 2012), the mechanisms and principal drivers of HEF have been studied in reduced-complexity flume experiments reproducing a series of triangular dunes (Fehlman, 1985; Elliott & Brooks, 1997; Salehin et al., 2004; Arnon et al., 2010; Fox et al., 2014; Blois et al., 2014), and using numerical modelling (Cardenas & Wilson, 2007a,b; Gomez et al., 2012; Jesson et al., 2013; Trauth et al., 2013; Gomez-Velez et al., 2014). The main mechanism of hyporheic exchange has been identified as the hydraulic forcing of the streamflow acting on the upstream side of a dune, which causes streamwater downwelling at the upstream side of the dune and upwelling further downstream.

Numerical models routinely follow the approach of modelling surface flow via the Navier-Stokes equation, whilst groundwater flow is modelled through a Darcy solver. A limitation of current approaches consists of the fact that turbulence in the surface flow is modelled through time-averaging techniques (Reynolds-Averaged Navier-Stokes, RANS) which remove the depencence of turbulent phenomena over time, instead of time-dependent approaches (viz.: Large Eddy Simulations, LES)—this despite the fact that short-timed perturbations are shown to affect HEF; for instance, dissolved oxygen conditions respond over time scales of hours-to-days when subjected to practically instantaneous surface flow perturbations (Kaufman et al., 2017). Furthermore, with few exceptions (Li et al., 2020), surface-groundwater coupling occurs one-way only, from surface to groundwater. surface flow is typically solved first; then, the output pressure field across the riverbed is informed to a separate simulations for groundwater flow as a boundary condition, with no mass transfer between surface and groundwater flows.

The aim of this work is to introduce the first-ever Lattice-Boltzmann (LB) numerical model, which specifically addressed the two limitations mentioned above. contrarily to the work mentioned above, single numerical runs simulate both surface and groundwater flows as part of the same computational domain, the difference between the two zones being defined only in terms of local porosity and permeability fields. this allows simultaneous, time-dependent resolution of surface and groundwater flow, as well as mass transfer. The Lattice-Boltzmann methodology (Kruger et al., 2017) was adopted because of its superior performance in terms of high numerical efficiency and parallelizability: indeed, previous work in other disciplines shows that lattice-Boltzmann outperforms Finite-Volume analogues by a factor of 100—1000 (Dapelo et al., 2019, 2020), and OpenLB's implementation of Lattice-Boltzmann (www.openlb.net) has been shown to maintain effective weak scaling over more than 10,000 cores (M. J. Krause et al., 2021).

Results show a time-dependent variation of the morphology of the hyporheic zone, which shrinks and extends possibly beyond the limits of a single beform element over short time periods. This behaviour, which is attributed to the time-dependent nature of the simulations presented here, was never observed in previous numerical work, and is in qualitative agreement with complex, short-timed flow variations observed in Direct Numerical Simulations

(DNS) work over reduced-sized computational domains (Shen et al., 2020, 2022). Also, the pressure field across the riverbed is shown to drop smoothly leeward of the bedform element. This is in contrast to previous numerical work (Cardenas & Wilson, 2007a,b; Gomez et al., 2012; Jesson et al., 2013; Trauth et al., 2013; Gomez-Velez et al., 2014), where a sharp cusp was observed, but in agreement with historical experimental observations (Fehlman, 1985). A more recent experimental work (Blois et al., 2014) shows that sharp cusps in riverbed pressure occur when no mass exchange is allowed between surface and groundwater flows, whilst smooth drops are observed when mass exchange is allowed. The model presented here qualitatively captures this behaviour.

In Section 2, the model and numerical setup are presented. The results are reported in Section 3. Conclusions are reported in Section 4.

2 Methods

2.1 Numerical Model

2.1.1 The Lattice-Boltzmann Method

The Lattice-Boltzmann is a mesoscopic method insofar as the macroscopic observable fields (viz.: pressure p, density ρ, velocity $\mathbf{u}$ and shear rate σ) are not solved directly; what is actually solved is a statistical quantity—the probability $f(\mathbf{x}, \mathbf{c}, t)$ of finding an abstract particle-like portion of fluid with position within $[\mathbf{x}, \mathbf{x}+\delta\mathbf{x}]$, velocity within $[\mathbf{c}, \mathbf{c}+\delta\mathbf{c}]$ and at a time within $[t, t+\delta t]$. Then, the macroscopic observable fields are calculated as f's first three momenta:

$$\rho := \int f\, d\mathbf{c}\,; \qquad \rho\mathbf{u} := \int f\mathbf{c}\, d\mathbf{c}\,; \qquad \rho\mathbf{u}\otimes\mathbf{u} := \sigma + \int f\mathbf{c}\otimes\mathbf{c}\, d\mathbf{c} \tag{1}$$

where $\otimes$ is the tensor product. f evolves according to a conservation equation in the phase space:

$$\left(\partial_t + \mathbf{c}\cdot\nabla\right) f = \mathscr{C}\left[f\right] \tag{2}$$

where the "collision operator" $\mathscr{C}$ accounts for inter-particle collisions. Under diluted gas conditions (which hold for riverine flows), only binary conditions are relevant. Furthermore, under the Bhatnagar-Gross-Krook (BGK) hypothesis Bhatnagar et al. (1954), binary collisions are assumed to occur isotropically and bear the effect of relaxing f towards a Maxwell equilibrium distribution f^{eq}:

$$\mathscr{C}\left[f\right] = -\frac{f - f^{(\mathrm{eq})}}{\tau} \tag{3}$$

and f^{eq} is defined as:

$$f^{(\mathrm{eq})}\left(\mathbf{x},\,t\right) := \rho\left(\mathbf{x},\,t\right)\left(\frac{1}{2\pi c_{\mathrm{s}}^{2}}\right)^{3/2}\exp\left\{-\frac{\left[\mathbf{u}\left(\mathbf{x},\,t\right)\right]^{2}}{2c_{\mathrm{s}}^{2}}\right\}\ , \tag{4}$$

where c_{S} is the sound speed.

Time and space are discretized in respectively in a succession of times of timesteps δt, and in a cubic lattice of size δx. Velocity is discretized by allowing only a small set of discrete velocities $\mathbf{c}_i$, $i = 0,\,\ldots,\,p-1$, symmetrically directed from a given lattice site to its first, second or third neighbour, and with magnitude 0, $\sqrt{1}$, $\sqrt{2}$, $\sqrt{3}$, ... times $\delta x/\delta t$. Different choices of space dimensionality and velocity discretization (schemes) are available, and are conventionally labelled as DnQp. After discretization, the continuous quantity $f\left(\mathbf{x},\,\mathbf{c},\,t\right)$ is converted to a set $f_i\left(\mathbf{x},\,t\right)$, each representing the probability of finding a fluid particle at the site $\mathbf{x}$ with velocity $\mathbf{c}_i$. The speed of sound c_{s} is porportional to $\delta x/\delta t$, with the constant of proportionality depending on the choice of lattice. Equarion 1 becomes:

$$\rho := \sum_i f_i\ , \qquad \rho\mathbf{u} := \sum_i \mathbf{c}_i f_i\ , \qquad \rho\mathbf{u}\otimes\mathbf{u} := \sigma + \sum_i \mathbf{c}_i\otimes\mathbf{c}_i\, f_i\ ; \tag{5}$$

Equation 2 bocomes:

$$f_i(\mathbf{x}+\mathbf{c}_i\delta t,\ t+\delta t) - f(\mathbf{x},\ t) = \mathscr{C}_i(\mathbf{x},\ t)\ ; \tag{6}$$

and Equation 3:

$$\mathcal{C}_i(\mathbf{x},\ t) = -\frac{1}{\tau}\left[f_i(\mathbf{x},\ t) - f_i^{\mathrm{eq}}(\mathbf{x},\ t)\right]\ . \tag{7}$$

The velocity discretization error is removed by writing f^{eq} as a series of Hermite polynomials. The Truncation to the second order reads as follows:

$$f_i^{\mathrm{eq}} = t_i\,\rho\left[1 + \frac{\mathbf{u}\cdot\mathbf{c}_i}{c_{\mathrm{s}}^2} + \frac{\left(\mathbf{u}\cdot\mathbf{c}_i\right)^2 - c_{\mathrm{s}}^2u^2}{2c_{\mathrm{s}}^4}\right] \tag{8}$$

and is shown through Chapman-Enskog perturbative analysis (Kruger et al., 2017) that it grants conservation of mass and momentum, and allows the reformulation of Equation 6 into weakly-compressible Navier-Stokes equations (Kruger et al., 2017), with macroscopic pressure and kinematic viscosity being respectively defined as:

$$p := \rho c_{\mathrm{s}}^2\ , \qquad \nu := c_{\mathrm{s}}^2\left(\tau - \frac{1}{2}\right)\delta t\ . \tag{9}$$

The truncation error corresponds to a small compressibility error and is proportional to Ma^2, with $\mathrm{Ma} \equiv \left|\mathbf{u}\right|/c_{\mathrm{s}}$ being the Mach number and $|\mathbf{u}|$ the problem's velocity scale. In low-Mach number problems (such as the one presented in this work), the solution is not affected by the actual value of Ma, as long as the condition Ma $\ll 1$ is observed. This allows the use of Ma, δx and δt as tuning parameters to strike the best balance between, accuracy, incompressibility and computational expense (Kruger et al., 2017).

2.1.2 Representative-Elementary-Volume (REV) porosity Model for Lattice-Boltzmann

The method described in Section 2.1.1 can be adapted to describe flows through porous media. Guo & Zhao (2002) proposed a REV model, where the pore structure is represented by a scalar field $\varepsilon(\mathbf{x},\, t) \in (0,\, 1)$, called porosity, with $\varepsilon = 0$ representing a solid node, and $\varepsilon = 1$ a free-flowing fluid node. Guo & Zhao (2002) also introduced a Darcy force:

$$\mathbf{F} = -\frac{\varepsilon\nu}{K}\mathbf{u}\,, \tag{10}$$

where K is the permeability coefficient. The equilibrium density function (Equation 8) is modified as follows:

$$f_i^{\mathrm{eq}} = t_i\,\rho\left[1 + \frac{\mathbf{u}\cdot\mathbf{c}_i}{c_\mathrm{s}^2} + \frac{(\mathbf{u}\cdot\mathbf{c}_i)^2 - c_\mathrm{s}^2 u^2}{2\varepsilon c_\mathrm{s}^4}\right]\,, \tag{11}$$

and a force term is added to the collision operator in the lattice-Boltzmann equation (Equation 6):

$$f_i(\mathbf{x} + \mathbf{c}_i\delta t,\ t + \delta t) - f(\mathbf{x},\ t) = \mathscr{C}_i(\mathbf{x},\ t) + \Phi_i\delta t\,. \tag{12}$$

The force term Φ_i is defined as follows:

$$\Phi_i = t_i\,\rho\left(1 - \frac{1}{2\tau}\right)\left[\frac{\mathbf{F}\cdot\mathbf{c}_i}{c_\mathrm{s}^2} + \frac{(\mathbf{u}\cdot\mathbf{c}_i)\,(\mathbf{F}\cdot\mathbf{c}_i) - c_\mathrm{s}^2\,\mathbf{u}\cdot\mathbf{F}}{\varepsilon c_\mathrm{s}^4}\right]\,. \tag{13}$$

The fluid velocity is no longer the first-order momentum density as it was in Equation 5. Rather, it is defined as:

$$\mathbf{u} := \sum_i \mathbf{c}_i f_i + \frac{1}{2}\rho\mathbf{F}\,\delta t\,. \tag{14}$$

Through a Chapman-Enskog expansion and the approximation of constant density, from the model described above it is possible to recover the following governing equations:

$$\begin{aligned} \nabla\cdot\mathbf{u} &= 0\,, \\ \partial_t\mathbf{u} + (\mathbf{u}\cdot\nabla)\,\frac{\mathbf{u}}{\varepsilon} &= -\nabla\,(\varepsilon p) + \nu\nabla^2\mathbf{u} + \mathbf{F}\,. \end{aligned} \tag{15}$$

Equations 15 were proposed by Nithiarasu et al. (1997) to describe flow through porous media of both constant and variable porosity. Equations 15 reduces to the Navier-Stokes equations when $\varepsilon \to 1$. It is also easy to recognise terms reproducing Darcy (Equation 10, first term on the right side), Brinkmann (Equation 15, second term on the right side) and

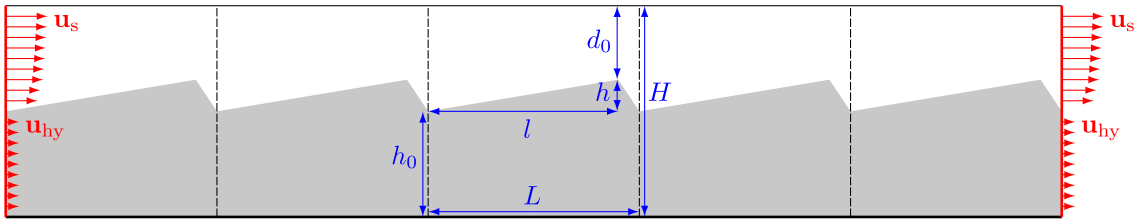

Figure 1: Schematic representation and boundary conditions of the computational domain. Bottom: no slip. Top: free slip. Leftmost and rightmost vertical boundaries: constant velocity.

Forchheimer (Equation 10, second term on the right side) models. This makes the model capable of describing free flow as well as flow through porous media with flexibility especially in the case of varying porosity, eventually capturing the effects of solid boundaries (through the Brinkmann component), or of non-linear drag (Forchheimer).

2.2 Meshing

2.2.1 Physics and Geometry

Two two-dimensional computational domains were defined as in Figure 1. The domain consisted of a succession of five identical dunes in order to mimic an infinite domain. The third dune was considered to be far away enough from the inlet and outlet to ignore boundary effects, and was used for the numerical predictions. In each lattice node, the values of the particle density functions f_i were stored as described in Section 2.1.1. In addition, each cell also contained the values of the porosity ε and the permeability K as scalar fields. The porosity field was defined in such a way to model a succession of dunes (filled in grey in Figure 1) overlaid by a free-flowing water column. The geometry of the dunes is reported in Table 1, and follows Gomez-Velez et al. (2014).

Following Pamuk & Özdemir (2012), porosity and permeability were chosen as $\varepsilon = 0.35$ and $K = 10^{-10}$ m^2 to reproduce the characteristics of sand. The kinematic viscosity of water was set to 10^{-6} m^2/s for the sake of simplicity. This value approximates the water kinematic viscosity at 20 °C of 1.004 10^{-6} m^2/s with a difference of less than 0.5%. The Reynolds

Table 1: Domain geometry.

L	(m)	1
l/L	(–)	0.9
h/L	(–)	0.075
d_0/L	(–)	0.425

number rwas $\sim 10^5$ and, consequently, a turbulence model was needed. A Smagorinsky large eddy simulations model (Hou et al., 1996) was adopted to reproduce the effect of turbulence. Cardenas & Wilson (2007a) used a definition of the Reynolds number where h is the relevant length scale. This choice may have been driven by the observation that the largest vortices appearing in the average figure (Figure 3) are apparently of the size of h. However, the correct reference length scale to define the Reynolds number is the one at which the gradients relevant to the problem occur (Kruger et al., 2017). Channel flow in average follows a sixth-power law, with horizontal gradients changing uniformly across the whole depth of the surface flow d_0. As such, d_0 and not h should be considered as the relevant length scale to define the Reynolds number.

The inlet surface average velocity was set to $u_{\mathrm{s}} = 0.3$ m/s, corresponding to a Froude number of 0.15. u_{hy} assumed the values of $5 \cdot 10^{-7}\, u_{\mathrm{s}}$, $10^{-6}\, u_{\mathrm{s}}$, $2 \cdot 10^{-6}\, u_{\mathrm{s}}$, $5 \cdot 10^{-6}\, u_{\mathrm{s}}$, $10^{-5}\, u_{\mathrm{s}}$, $2 \cdot 10^{-5}\, u_{\mathrm{s}}$, $5 \cdot 10^{-5}\, u_{\mathrm{s}}$, $10^{-4}\, u_{\mathrm{s}}$. The choice of these value is justified *a posteriori* by the fact that they allow to capture a qualitative change in the hyporheic zone morphology.

The boundary conditions consisted of a non-periodic domain with constant velocity at the inlet and the outlet defined according to a sixth power with average velocity u_{s} law in the surface zone, and a constant value u_{hy} in the hyporheic zone:

$$u = \begin{cases} u_{\mathrm{hy}} \,, & 0 \le d \le h_0 \,; \\ \left(\dfrac{d - h_0}{H - h_0}\right)^{1/6} u_s \,, & h_0 < d \le H \,. \end{cases} \tag{16}$$

2.2.2 Numerical Setup

The D2Q9 lattice scheme was adopted. In such a scheme, four horizontal velocities (pointing to the first neighbours), four diagonal (to the second neighbours) and a zero velocity are defined, and the lattice sound speed is $\delta x / \big(\sqrt{3}\, \delta t\big)$.

The implementation of the model described in Section 2.1.2 produced a stepwise variation of the porosity field ε across the dune slopes; this, in turn, resulted into unphysical oscillations of the instant values of the pressure across the riverbed with a period of the order of magnitude of the step's amplitude. To minimise this effect, a fine grid was needed, an accordingly, a regular grid with 800 nodes per metre was adopted, with an overall node number of 6.4 million. furthermore, the choice of adopting a low value for K meant that groundwater velocity magnitude was several orders of magnitude smaller than in the surface stream. As such, the truncation error described in Section 2.1.1 (and consequently, the Mach number Ma) needed to be kept as low as possible. As such, the time step δt was chosen in such a way that $u_s = 0.01\,\delta x/\delta t$, thus obtaining $\mathrm{Ma} = 0.0173 \ll 1$. Each simulation was run in parallel on four to five dual-processor 8-core 64-bit 2.2 GHz Intel Sandy Bridge E5-2660 worker nodes with 32 GB of memory, for a total of 62 and 80 nodes respectively. Each run required 30 to 60 hours of real time. Furure work will reduce the present model's computational demand by: *(i)* introducing a smooth surface-groundwater transition for the porosity field ε, thus reducing unphysical pressure oscillations across the riverbed and, consequently, the need for fine grids; and *(ii)* adopting higher values for K, as in Blois et al. (2014).

60 to 210 s of simulated time were reproduced to keep track of the long-term behaviour of the computational model. Then, the initial transient period, consisting of the first 10 s of simulated time, was discarded, and the remaining time steps were averaged node by node to produce an averaged velocity field for post-processing.

3 Results and Discussion

3.1 Grid convergence

Grid independence was assessed on an *ad hoc* modified version of the setting described in Section 2.2: where more meshes are considered (viz.: with 1130, 800, 566 and 400 grid points per metre respectively), the choice of u_{hy} was limited to $10^{-6}\,u_{\mathrm{s}}$, and the computational domain was enlarged to 6 dunes, the third of which was considered for the test results. The Grid Convergence Index (GCI) test (Roache, 1994; Celik et al., 2008) was performed on the measure of the hyporheic depth. The results of the test showed that grid independence was achieved across all the four meshes, that the mesh with 800 grid points per metre was the best compromise between accuracy and numerical expense, and that the relative error in results produced through that grid was about 3%.

3.2 Pressure propagation through the Riverbed

Figure 2 shows the pressure propagation through the riverbed surface for $u_{\mathrm{hy}} = 10^{-6}\, u_{\mathrm{s}}$. The pressure profile is obtained by averaging the instantaneous values of the pressure at each point of the riverbed over 200 s, as per in Section 2.2.2) and then, compared to literature values previously reported by Gomez-Velez et al. (2014) (Figure 2, left). Pressure oscillations

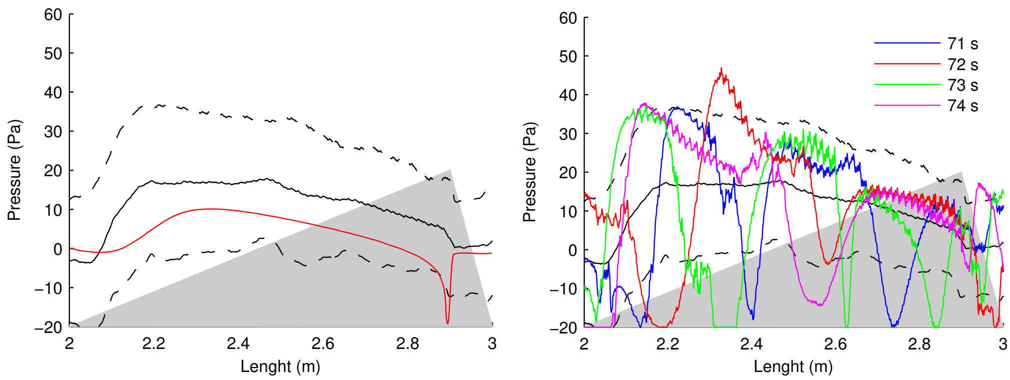

Figure 2: Pressure through the riverbed. Left: average (black) plus and minus standard deviation (dashed); Comparison with literature data of Gomez-Velez et al. (2014) (red). Right: timestep snapshots at 71, 72, 73 and 74 s.

were observed as described in Section 2.2.2, but their magnitude was reduced if compared to the main trend. The simulation results display a strong time-dependence, as shown by the large standard deviation, and the example timesteps reported in Figure 2, right. Simulation results show a smooth pressure drop leeward of the bedform, like the experimental results of Fehlman (1985). In contrast, previous numerical work (Cardenas & Wilson, 2007a,b; Gomez et al., 2012; Jesson et al., 2013; Trauth et al., 2013; Gomez-Velez et al., 2014; Lee et al., 2021) display a sharp peak (the result from Gomez-Velez et al. (2014) are reported in Figure 2 as an example).

This qualitatively different behaviour may be explained considering the results of the experiments conducted by Blois et al. (2014). It is therein shown that a sharp peak occurs when no mass exchange between surface and groundwater flows is allowed (as in the above-mentioned previous numerical work); by contrast, even a tiny exchange flow is shown to smooth out the sharp peak into a smooth pressure drop (as in the numerical results reported within this article). This hypothesis is corroborated by the experimental observation (Blois et al., 2014) that surface-groundwater mass exchange prompts qualitatively different surface flow patterns leeward of the bedform element, if compared to the case where no exchange flow is allowed (viz.: flow reattachment does not occur). Groundwater flow in Blois et al. (2014) occurs through coarse sediments modelled as a cubical lattice of spherical spheres of 1 cm diameter, corresponding to a porosity $\varepsilon = 1 - \pi/6 = 0.476$, of the same order of magnitude of the porosity considered within this work, and a permeability of $K = \varepsilon^3 D^2 / \left[150\,(1-\varepsilon)^2\right] = 3.797 \cdot 10^{-6}$ m^2, around four orders of magnitude larger than the permeability used within this study. As such, this study suggest that Blois et al. (2014)'s conclusions apply at least to a certain extent, to much finer sediments.

3.3 Velocity Patterns and Hyporheic depth

Figure 3 reports the average flow patterns of surface (top row) and hyporheic flow (bottom row). The averaging procedure was performed as per in Section 2.2.2. HEF patterns

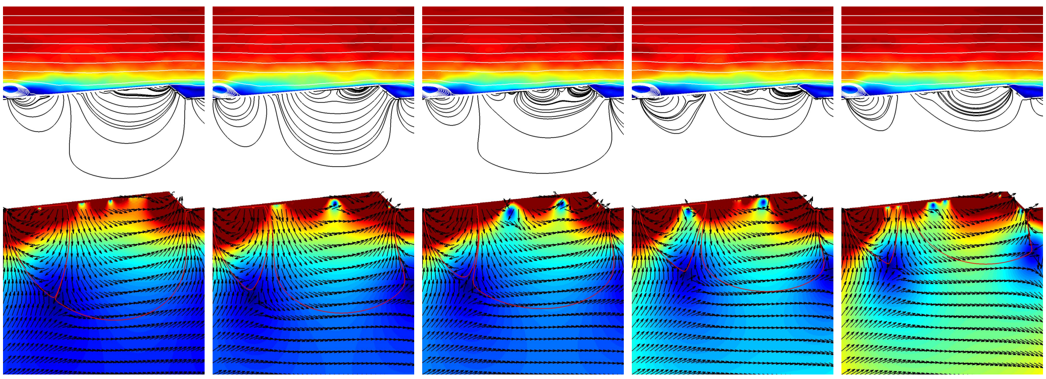

Figure 3: Fluid flow average figure. Top row: surface velocity magnitude and surface-hyporheic streamlines, velocity cutoff: 0.6 m/s. From left to right: $u_{\mathrm{hy}} = 5 \cdot 10^{-6}\, u_{\mathrm{s}}$, $u_{\mathrm{hy}} = 10^{-5}\, u_{\mathrm{s}}$, $u_{\mathrm{hy}} = 2 \cdot 10^{-5}\, u_{\mathrm{s}}$, $u_{\mathrm{hy}} = 5 \cdot 10^{-5}\, u_{\mathrm{s}}$, $u_{\mathrm{hy}} = 10^{-4}\, u_{\mathrm{s}}$. Bottom row: Patterns of hyporheic flow velocity and limits of the hyporheic zone, velocity cutoff: 10^{-5} m/s. From left to right: $u_{\mathrm{hy}} = 5 \cdot 10^{-7}\, u_{\mathrm{s}}$, $u_{\mathrm{hy}} = 10^{-5}\, u_{\mathrm{s}}$, $u_{\mathrm{hy}} = 2 \cdot 10^{-5}\, u_{\mathrm{s}}$, $u_{\mathrm{hy}} = 5 \cdot 10^{-5}\, u_{\mathrm{s}}$, $u_{\mathrm{hy}} = 10^{-4}\, u_{\mathrm{s}}$.

are in general agreement with those previously reported by using other modelling methodologies, such as in Cardenas & Wilson (2007a). The surface flow simulated in this study displays a certain degree of regularity, with (turbulent) horizontal flow and velocity increasing with the height from the bottom; a persistent vortex is present after the tip of the dune, with an apparent flow separation. No dependence on u_{hy} is visible.

The hyporheic flow patterns indicate the existence of a down-welling point at around 1/3 of the dune slope before the tip, and a diffuse up-welling zone in the receding zone after the tip of the dune. Curved streamlines connect the down-welling point and the up-welling zone, with the flow patterns becoming less intensive as the depth increases.

No perceivable or weak dependence on u_{hy} is visible as long as $u_{\mathrm{hy}} \lesssim 2 \cdot 10^{-5}\, u_{\mathrm{s}}$. Above that value, the increase of u_{hy} produces an intensification of the hyporheic flow patterns. At the same time, the hyporheic zone contracts. This observation above is corroborated by the quantitative calculations of hyporheic depth, area, velocity and residence time. The data are reported in Table 2 and plotted in Figure 4. Below the threshold value of $u_{\mathrm{hy}} \lesssim 2 \cdot 10^{-5}\, u_{\mathrm{s}}$, hyporheic velocity displays fluctuations, while hyporheic depth, area and residence time show a weak descending trend. Above such threshold, all the quantities present a strong descending trend.

Table 2: Hyporheic depth, area of the hyporheic zone, average hyporheic velocity and average residence time. $u_{\mathrm{hy}} = 10^{-6}\, u_{\mathrm{s}}$.

u_{hy}	d_{hy} (m)	A_{hy} (m^2)	$\langle v \rangle_{\mathrm{hy}}$ (mm/s)	$\langle t \rangle_{\mathrm{hy}}$ (days)
$5 \cdot 10^{-7}\, u_{\mathrm{s}}$	0.469	0.412	0.506	1,150
$10^{-6}\, u_{\mathrm{s}}$	0.483	0.426	0.472	1,190
$2 \cdot 10^{-6}\, u_{\mathrm{s}}$	0.478	0.423	0.436	1,080
$5 \cdot 10^{-6}\, u_{\mathrm{s}}$	0.453	0.403	0.482	1,110
$10^{-5}\, u_{\mathrm{s}}$	0.439	0.392	0.501	935
$2 \cdot 10^{-5}\, u_{\mathrm{s}}$	0.420	0.387	0.502	997
$5 \cdot 10^{-5}\, u_{\mathrm{s}}$	0.348	0.303	0.588	621
$10^{-4}\, u_{\mathrm{s}}$	0.232	0.207	0.982	434

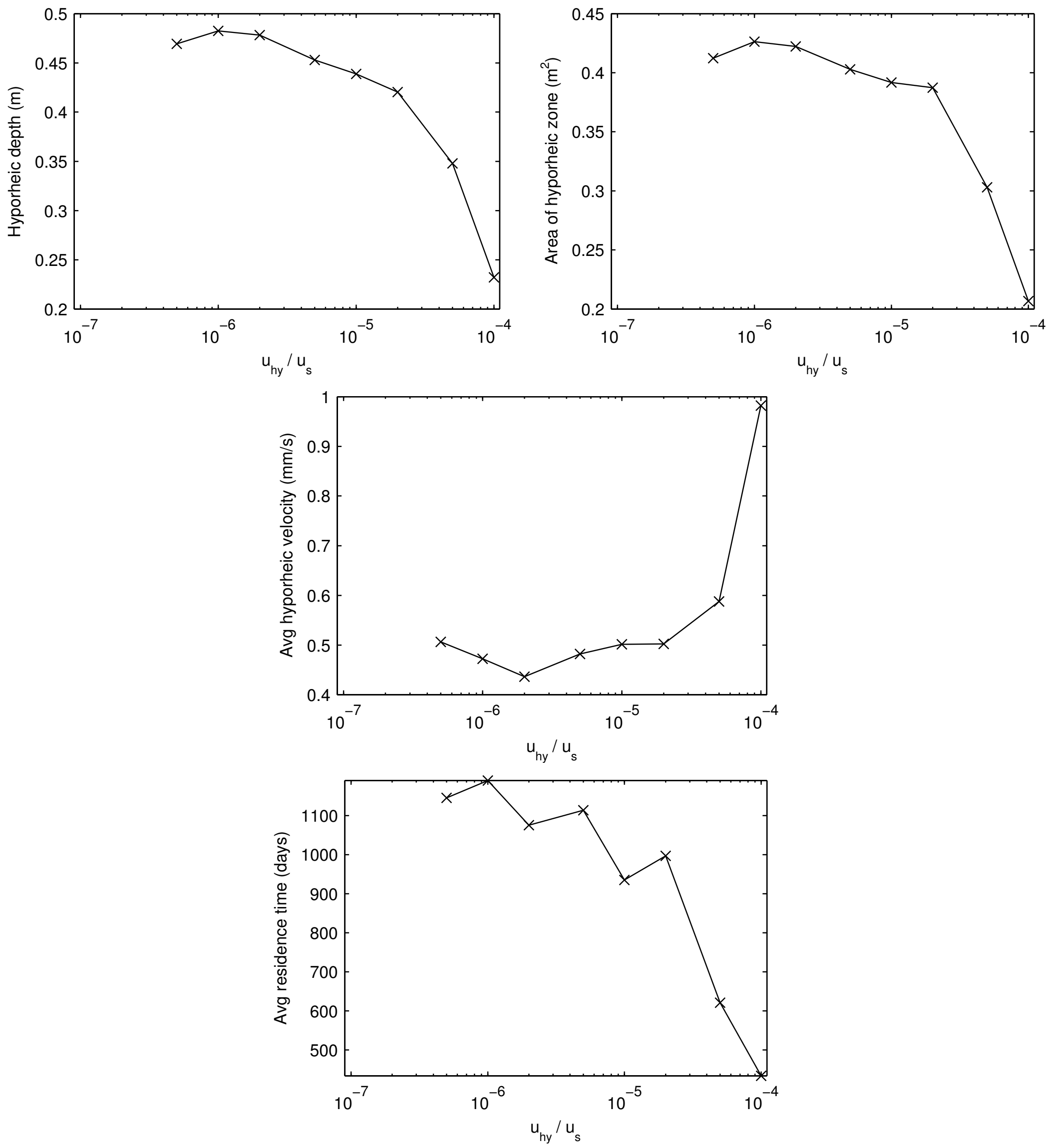

Figure 4: Hyporheic hepth, area of hyporheic zone, average hyporheic velocity and average residence time against u_{hy} to u_{s} ratio. Logarithmic plot. $u_{\mathrm{hy}} = 10^{-6}\, u_{\mathrm{s}}$.

It is clear that the choice of how to set the magnitude of the hyporheic boundary velocity $\mathbf{u}_{\mathrm{hy}}$ affects the outcome of the simulations, for higher velocities as the hyporheic zone is "squeezed" by an external horizontal flux, as can be seen from Figure 3. In this context, the meaning of "higher velocities" and, conversely, "lower velocities", is provided by comparing the choice of u_{hy} to the values of the average hyporheic velocity. More precisely, "higher" values of u_{hy} means "u_{hy} larger than 1/10 of the average hyporheic velocity".

3.4 Time-Dependant Evolution and Turbulence

In Figure 5, the time evolution of the hyporheic depth and the area of the hyporheic zone are reported. The behaviour of the case $u_{\mathrm{hy}} = 10^{-6}\, u_{\mathrm{s}}$ has been reported as an example

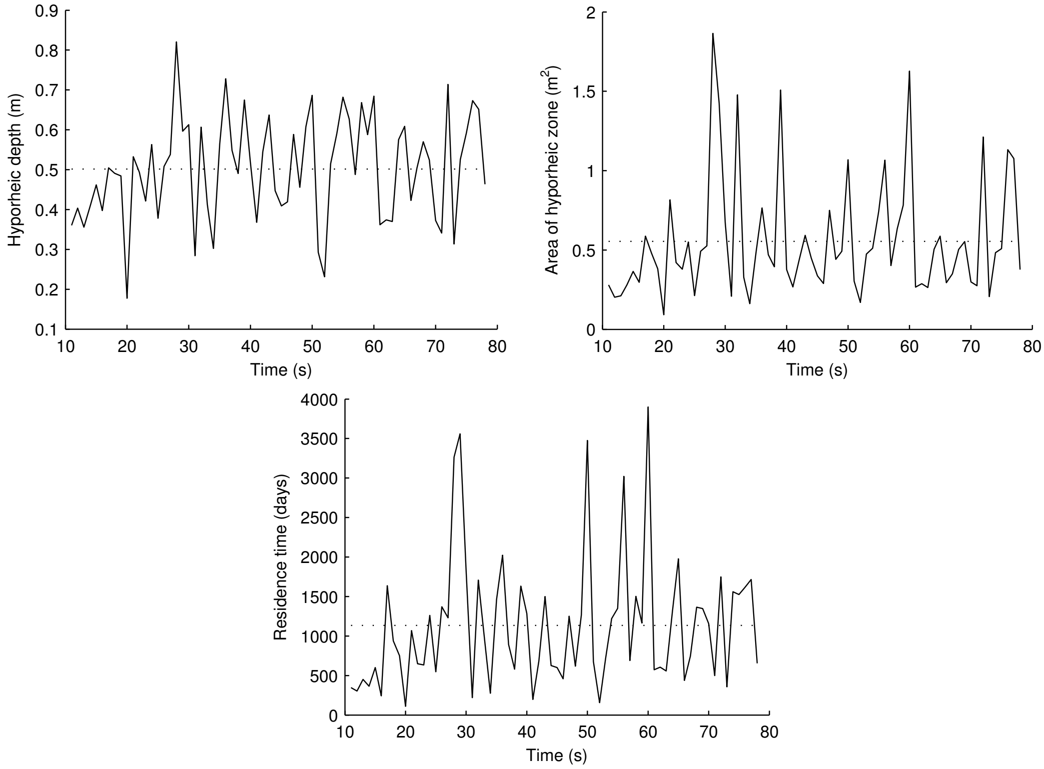

Figure 5: Hyporheic depth, area of hyporheic zone and residence time over time. $u_{\mathrm{hy}} = 10^{-6}\, u_{\mathrm{s}}$.

here. The values of Hyporheic depth, area and residence time present strong oscillations over time. This suggests that the instantaneous values of hyporheic depth, area and residence time may be influenced by the time variability of the flow patterns. To corroborate this claim, the instantaneous values of the flow patterns are taken into consideration in the following part of this work.

Figure 6 shows surface velocity magnitude and instantaneous streamlines at different time steps, while in Figure 7 the instantaneous hyporheic flow patterns are reported. Both surface and hyporheic velocity patterns display strong time dependence.

A comparison between Figure 3 and Figures 6 shows that the instantaneous surface flow patterns are much more complex than their average field, as they comprise strong

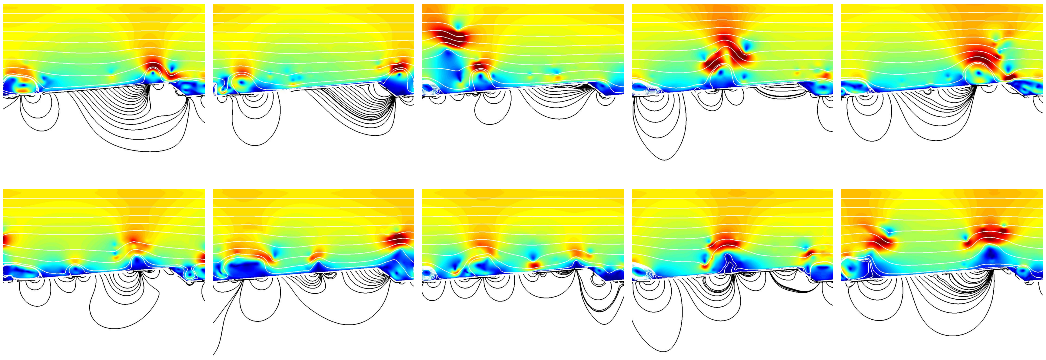

Figure 6: Surface velocity magnitude and surface-hyporheic streamlines. Velocity cutoff: 0.6 m/s. $u_{\mathrm{hy}} = 10^{-6}\, u_{\mathrm{s}}$. From left to right and from top to bottom: snapshot figures at: 11 s, 12 s, 13 s, 14 s, 15 s, 71 s, 72 s, 73 s, 74 s and 75 s.

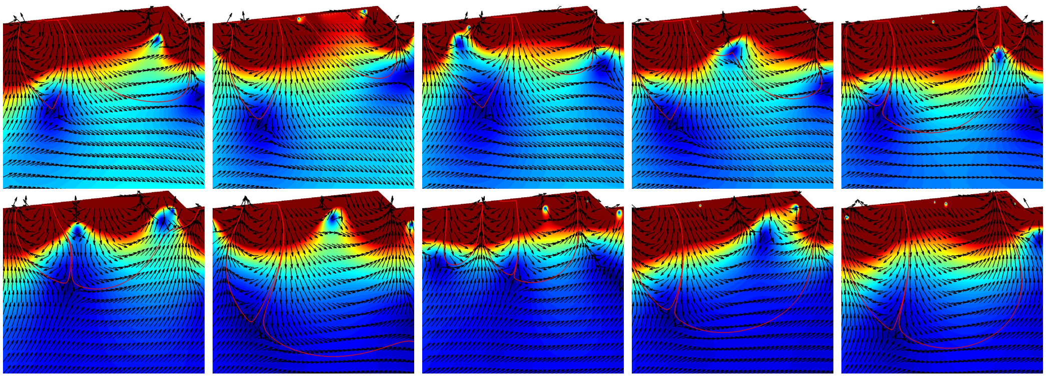

Figure 7: Hyporheic flow patterns. Velocity cutoff: 10^{-5} m/s. $u_{\mathrm{hy}} = 10^{-6}\, u_{\mathrm{s}}$. From left to right and from top to bottom: snapshot figures at: 11 s, 12 s, 13 s, 14 s, 15 s, 71 s, 72 s, 73 s, 74 s and 75 s.

time-dependent structures interpretable as transient vortices flowing with the stream, and unstable flow separation at the tip of the dune. In the case of average fluid flow fields (Figure 3), those patterns are not apparent as they have been averaged out over the simulation period.

The snapshots of the hyporheic flow patterns shown in (Figure 7) reveal more similarity with the average figure (Figure 2). However, it is possible to appreciate that downwelling and upwelling points change over time—in particular, they tend to be located below transient vortices in the surface flow.

The deepest hyporheic structures similarly reveal time dependence. The shape of the hyporheic zone does change over time—in particular, the hyporheic zone can comprise more than one dune extending beyond a single streamed feature, as shown in Figure 8. A more complex structure of nested vortices and long-range connections is depicted. In conclusion,

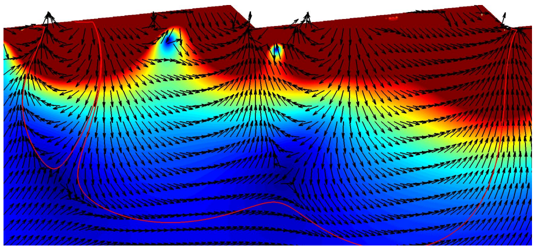

Figure 8: Hyporheic flow patterns. Velocity cutoff: 10^{-5} m/s. $u_{\mathrm{hy}} = 10^{-6}\, u_{\mathrm{s}}$. Snapshot figure at 72 s.

Figure 6 and 7 show that the time-dependent turbulent structure of the surface flow influences the hyporheic flow patterns significantly, and that their influence is expected to become less relevant with increasing depth. However, further work is necessary to quantify this influence.

4 Conclusions

The first-ever Lattice-Boltzmann model for hyporheic exchange fluxes across groundwater-surface water interfaces is presented. Elements of novelty include transient simulation process, and surface-groundwater two-way mass flux.

The introduction of surface-groundwater two-way mass flux leads to more accurate predictions of pressure across the riverbed than previous numerical models, and allows to explain the qualitative behaviour of leeway pressure drop in terms of mass flow exchange.

The time-dependent nature of the model allow to capture short-time-dependent fluctuations in hyporheic zone's area, shape, extent and average velocity, which were not previously predicted. Experimental work will be necessary to verify the accuracy of these predictions.

Acknowledgments

D.D was funded by the NERC grant NE/L003872/1 . J.D.G-V. was funded by the U.S. Department of Energy, Office of Science, Biological and Environmental Research. This work is a product of two programs: (i) Environmental System Science Program, as part of the Watershed Dynamics and Evolution (WADE) Science Focus Area (SFA) at ORNL and the IDEAS-Watersheds project, and (ii) Data Management Program, as part of the ExaSheds project. Additional support was provided by the National Science Foundation (awards EAR-1830172, OIA-2020814, and OIA-2312326). The code implemented for the analysis is publicly available under GNU GPL 2.0 license in the Supplementary Material.

References

Angermann, L., Krause, S., & Lewandowski, J. (2012, December). Application of heat pulse injections for investigating shallow hyporheic flow in a lowland river: HEAT PULSE INJECTIONS FOR INVESTIGATING HYPORHEIC FLOW. *Water Resources Research*, *48*(12). Retrieved 2022-11-25, from `http://doi.wiley.com/10.1029/2012WR012564` doi: 10.1029/2012WR012564

Arnon, S., Marx, L. P., Searcy, K. E., & Packman, A. I. (2010). Effects of overlying velocity, particle size, and biofilm growth on stream–subsurface exchange of particles. *Hydrological Processes*, *24*(1), 108–114. Retrieved from `http:https://doi.org/10.1002/hyp.7490` (Publisher: Wiley Online Library) doi: 10.1002/hyp.7490

Bhatnagar, P. L., Gross, E. P., & Krook, M. (1954). A model for collision processes in gases. I. Small amplitude processes in charged and neutral one-component systems. *Physical Review*, *94*(3), 511–525. (ISBN: 0031-899X) doi: 10.1103/PhysRev.94.511

Blois, G., Best, J. L., Sambrook Smith, G. H., & Hardy, R. J. (2014, September). Effect of bed permeability and hyporheic flow on turbulent flow over bed forms. *Geophysical Research Letters*, *41*(18), 6435–6442. Retrieved 2023-03-28, from `http://doi.wiley.com/10.1002/2014GL060906` doi: 10.1002/2014GL060906

Cardenas, M. B., & Wilson, J. L. (2007a). Dunes , turbulent eddies , and interfacial exchange with permeable sediments. *Water Resources Research*, *43*, 1–16. doi: 10.1029/2006WR005787

Cardenas, M. B., & Wilson, J. L. (2007b). Hydrodynamics of coupled flow above and below a sediment-water interface with triangular bedforms. *Advances in Water Resources*, *30*(3), 301–313. (ISBN: 0309-1708) doi: 10.1016/j.advwatres.2006.06.009

Celik, I. B., Ghia, U., Roache, P. J., Freitas, C. J., Coleman, H., & Raad, P. E. (2008). Procedure for Estimation and Reporting of Uncertainty Due to Discretization in CFD Applications. *Journal of Fluids Engineering*, *130*(7), 078001. doi: 10.1115/1.2960953

Dapelo, D., Trunk, R., Krause, M. J., & Bridgeman, J. (2019). Towards Lattice-Boltzmann modelling of unconfined gas mixing in anaerobic digestion. *Computers and Fluids*, *180*, 11–21. Retrieved from `https://doi.org/10.1016/j.compfluid.2018.12.008` (Publisher: Elsevier Ltd) doi: 10.1016/j.compfluid.2018.12.008

Dapelo, D., Trunk, R., Krause, M. J., Cassidy, N., & Bridgeman, J. (2020). The application of Buckingham pi theorem to Lattice-Boltzmann modelling of sewage sludge digestion. *Computers and Fluids*, *209*, 104632. Retrieved from `https://doi.org/10.1016/j.compfluid.2020.104632` (Publisher: Elsevier Ltd) doi: 10.1016/j.compfluid.2020.104632

Elliott, A. H., & Brooks, N. H. (1997, January). Transfer of nonsorbing solutes to a streambed with bed forms: Laboratory experiments. *Water Resources Research*, *33*(1), 137–151. Retrieved from `http://doi.wiley.com/10.1029/96WR02783` doi: 10.1029/96WR02783

Fehlman, H. M. (1985). *Resistance components and velocity distributions of open channel flows over bedforms* (Unpublished doctoral dissertation). Colorado State University.

Fox, A., Boano, F., & Arnon, S. (2014). Impact of losing and gaining streamflow conditions on hyporheic exchange fluxes induced by dune-shaped bed forms. *Water Resources Research*, *50*(3), 1895–1907. Retrieved from `http:https://doi.org/10.1002/2013WR014668` (Publisher: Wiley Online Library ISBN: 1944-7973) doi: 10.1002/2013WR014668

Gomez, J. D., Wilson, J. L., & Cardenas, M. B. (2012). Residence time distributions in sinuosity-driven hyporheic zones and their biogeochemical effects. *Water Resources Research*, *48*(9), 1–17. (ISBN: 0043-1397) doi: 10.1029/2012WR012180

Gomez-Velez, J. D., Krause, S., & Wilson, J. L. (2014, June). Effect of low-permeability layers on spatial patterns of hyporheic exchange and groundwater upwelling. *Water Resources Research*, *50*(6), 5196–5215. Retrieved from `http://doi.wiley.com/10.1002/2013WR015054` doi: 10.1002/2013WR015054

Guo, Z., & Zhao, T. S. (2002). Lattice Boltzmann model for incompressible flows through porous media. *Physical Review E - Statistical, Nonlinear, and Soft Matter Physics*, *66*(3), 1–9. (ISBN: 1063-651X) doi: 10.1103/PhysRevE.66.036304

Hou, S., Sterling, J., Chen, S., & Doolen, G. D. (1996). A Lattice Boltzmann Subgrid Model for High Reynolds Number Flows. In A. Lawniczak: & R. Kapral (Eds.), *Pattern formation and lattice gas automata* (Vol. 6). AMS

- Fields Institute Communications. Retrieved from http://books.google.com/books?hl=en&lr=&id=TIdy6-ItW7YC&oi=fnd&pg=PA151&dq=A+Lattice+Boltzmann+Subgrid+Model+for+High+Reynolds+Number+Flows&ots=zqrEqXjMNL&sig=_76MYxU-XPd2n1iKsPD5rIJQ7-Q (arXiv: comp-gas/9401004)

Jesson, M., Sterling, M., & Bridgeman, J. (2013, February). Modeling Flow in an Open Channel with Heterogeneous Bed Roughness. *Journal of Hydraulic Engineering*, *139*(2), 195–204. Retrieved 2015-07-07, from http://ascelibrary.org/doi/abs/10.1061/(ASCE)HY.1943-7900.0000621 (Publisher: American Society of Civil Engineers) doi: 10.1061/(ASCE)HY.1943-7900.0000621

Kaufman, M. H., Cardenas, M. B., Buttles, J., Kessler, A. J., & Cook, P. L. M. (2017). Hyporheic hotmoments: Dissolved oxygen dynamics in the hyporheic zone in response to surface flow perturbations. *Water Resources Research*. doi: 10.1002/2016WR020296

Krause, M. J., Kummerlaender, A., Avis, S. J., Kusumaatmaja, H., Dapelo, D., Klemens, F., ... Simonis, S. (2021, January). OpenLB-Open source lattice Boltzmann code. *Computers and Mathematics with Applications*, *81*, 258–288. Retrieved from https://doi.org/10.1016/j.camwa.2020.04.033 (Publisher: Elsevier Ltd) doi: 10.1016/j.camwa.2020.04.033

Krause, S., Abbott, B. W., Baranov, V., Bernal, S., Blaen, P., Datry, T., ... Zarnetzke, J. P. (2022). Organizational Principles of Hyporheic Exchange Flow and Biogeochemical Cycling in River Networks Across Scales. *Water Resources Research*, *58*(3). Retrieved 2022-11-25, from https://onlinelibrary.wiley.com/doi/10.1029/2021WR029771 doi: 10.1029/2021WR029771

Krause, S., Tecklenburg, C., Munz, M., & Naden, E. (2013, March). Streambed nitrogen cycling beyond the hyporheic zone: Flow controls on horizontal patterns and depth distribution of nitrate and dissolved oxygen in the upwelling groundwater of a lowland river: NITROGEN CYCLING BEYOND THE HYPORHEIC. *Journal of Geophysical Research: Biogeosciences*, *118*(1), 54–67. Retrieved 2022-11-25, from http://doi.wiley.com/10.1029/2012JG002122 doi: 10.1029/2012JG002122

Kruger, T., Kasumaatmaja, H., Kuzmim, A., Shardt, O., Silva, G., & Viggen, E. M. (2017). *The lattice boltzmann method*. Springer. (arXiv: 1011.1669v3 Issue: March 2015 ISSN: 1098-6596) doi: 10.1007/978-3-319-44649-3

Lee, A., Aubeneau, A., Liu, X., & Cardenas, M. B. (2021, March). Hyporheic Exchange in Sand Dunes Under a Freely Deforming River Water Surface. *Water Resources Research*, *57*(3). Retrieved 2023-03-28, from https://onlinelibrary.wiley.com/doi/10.1029/2020WR028817 doi: 10.1029/2020WR028817

Li, B., Liu, X., Kaufman, M. H., Turetcaia, A., Chen, X., & Cardenas, M. B. (2020, February). Flexible and Modular Simultaneous Modeling of Flow and Reactive Transport in Rivers and Hyporheic Zones. *Water Resources Research*, *56*(2). Retrieved 2023-03-28, from https://onlinelibrary.wiley.com/doi/10.1029/2019WR026528 doi: 10.1029/2019WR026528

Marçais, J., Gauvain, A., Labasque, T., Abbott, B. W., Pinay, G., Aquilina, L., ... de Dreuzy, J.-R. (2018, September). Dating groundwater with dissolved silica and CFC concentrations in crystalline aquifers. *Science of The Total Environment*, *636*, 260–272. Retrieved 2022-11-25, from https://linkinghub.elsevier.com/retrieve/pii/S0048969718313731 doi: 10.1016/j.scitotenv.2018.04.196

Nithiarasu, P., Seetharamu, K., & Sundararajan, T. (1997). Natural convective heat transfer in a fluid saturated variable porosity medium. *International Journal of Heat and Mass Transfer*, *40*(16), 3955–3967. (ISBN: 0017-9310) doi: 10.1016/S0017-9310(97)00008-2

Pamuk, M. T., & Özdemir, M. (2012). Friction factor, permeability and inertial coefficient of oscillating flow through porous media of packed balls. *Experimental Thermal and Fluid Science*, *38*, 134–139. doi: 10.1016/j.expthermflusci.2011.12.002

Roache, P. J. (1994). Perspective: a method for unifor reporting of grid refinement studies. *Journal of Fluids Engineering*, *116*, 405–413.

Salehin, M., Packman, A. I., & Paradis, M. (2004). Hyporheic exchange with heterogeneous streambeds: Laboratory experiments and modeling. *Water Resources Research*, *40*(11). Retrieved from http:https://doi.org/10.1029/2003WR002567 (Publisher: Wiley Online Library) doi: 10.1029/2003WR002567

Shen, G., Yuan, J., & Phanikumar, M. S. (2020, June). Direct numerical simulations of turbulence and hyporheic mixing near sediment–water interfaces. *Journal of Fluid Mechanics*, *892*, A20. Retrieved 2023-03-28, from https://www.cambridge.org/core/product/identifier/S0022112020001731/type/journal_article doi: 10.1017/jfm.2020.173

Shen, G., Yuan, J., & Phanikumar, M. S. (2022, April). Quantifying the Effects of Bed Roughness on Transit Time Distributions via Direct Numerical Simulations of Turbulent Hyporheic Exchange. *Water Resources Research*, *58*(4). Retrieved 2023-03-28, from https://onlinelibrary.wiley.com/doi/10.1029/2021WR030503 doi: 10.1029/

2021WR030503

Trauth, N., Schmidt, C., Maier, U., Vieweg, M., & Fleckenstein, J. H. (2013). Coupled 3-D stream flow and hyporheic flow model under varying stream and ambient groundwater flow conditions in a pool-riffle system. *Water Resources Research*, *49*(9), 5834–5850. doi: 10.1002/wrcr.20442

Wu, L., Gomez-Velez, J. D., Krause, S., Singh, T., Wörman, A., & Lewandowski, J. (2020, March). Impact of Flow Alteration and Temperature Variability on Hyporheic Exchange. *Water Resources Research*, *56*(3). Retrieved 2023-03-30, from https://onlinelibrary.wiley.com/doi/10.1029/2019WR026225 doi: 10.1029/2019WR026225

Zarnetske, J. P., Haggerty, R., Wondzell, S. M., & Baker, M. A. (2011, March). Dynamics of nitrate production and removal as a function of residence time in the hyporheic zone. *Journal of Geophysical Research*, *116*(G1), G01025. Retrieved 2022-11-25, from http://doi.wiley.com/10.1029/2010JG001356 doi: 10.1029/2010JG001356